Dark photons from the center of the Earth: Smoking-gun signals of dark matter

Jonathan L. Feng, Jordan Smolinsky, and Philip Tanedo

Dark Photons from the Center of the Earth: Smoking-Gun Signals of Dark Matter

Jonathan L. Feng[*], Jordan Smolinsky[†], and Philip Tanedo[‡]

Department of Physics and Astronomy,
University of California, Irvine, California 92697, USA

Abstract

Dark matter may be charged under dark electromagnetism with a dark photon that kinetically mixes with the Standard Model photon. In this framework, dark matter will collect at the center of the Earth and annihilate into dark photons, which may reach the surface of the Earth and decay into observable particles. We determine the resulting signal rates, including Sommerfeld enhancements, which play an important role in bringing the Earth's dark matter population to their maximal, equilibrium value. For dark matter masses $m_X \sim 100 \text{ GeV} - 10 \text{ TeV}$, dark photon masses $m_{A'} \sim \text{MeV} - \text{GeV}$, and kinetic mixing parameters $\varepsilon \sim 10^{-9} - 10^{-7}$, the resulting electrons, muons, photons, and hadrons that point back to the center of the Earth are a smoking-gun signal of dark matter that may be detected by a variety of experiments, including neutrino telescopes, such as IceCube, and space-based cosmic ray detectors, such as Fermi-LAT and AMS. We determine the signal rates and characteristics, and show that large and striking signals—such as parallel muon tracks—are possible in regions of the $(m_{A'}, \varepsilon)$ plane that are not probed by direct detection, accelerator experiments, or astrophysical observations.

[*] jlf@uci.edu
[†] jsmolins@uci.edu
[‡] flip.tanedo@uci.edu

I. INTRODUCTION

Dark matter may live in a dark sector with its own forces. This possibility has some nice features. For example, the dark matter's stability may be ensured not by some discrete parity imposed by hand, but simply by its being the lightest fermion in the dark sector. If the dark sector contains an Abelian gauge symmetry, dark electromagnetism, the dark photon and the Standard Model (SM) photon will generically mix kinetically. This mixing is of special interest because it is one of the few ways for a dark sector to interact with the known particles through a renormalizable interaction and it is non-decoupling: a particle charged under both dark and standard electromagnetism induces this interaction at loop-level, and the effect is not suppressed for very heavy particles. In this way, this is a prototype for simplified dark matter models with light mediators. The idea of a separate sector with its own photon [1, 2] and the further possibility of kinetic mixing between these two photons [3, 4] were first explored long ago, for dark matter detection have recently attracted widespread interest [5, 6].

In this framework, dark matter will collect in the center of the Earth and annihilate to dark photons $XX \to A'A'$. These dark photons may then travel to near the surface of the Earth and decay to SM particles, which may be detected in a variety of experiments, from under-ice/underwater/underground experiments, such as the current experiments IceCube, SuperK, and ANTARES, and future ones, such as KM3NeT, IceCube II, DUNE, and HyperK, to space-based cosmic ray detectors, such as the current experiments Fermi-LAT and AMS-02, and future ones, such as CALET, ISS-CREAM, and others. The resulting signals of electrons, muons, photons, and hadrons that point back to the center of the Earth are potentially striking signals of dark matter.

The possibility of dark matter signals from the centers of large astrophysical bodies was first proposed and investigated many years ago [7–16], and there have been important advances for the particular case of the Earth in recent years [17–25]. Typically these signals rely on annihilation to neutrinos, resulting in single-particle signals with a continuum of energies. In contrast, dark photons decay into two charged particles, which may be seen at the same time in a single experiment, and the total energy of these charged particles is equal to the dark matter particle's mass, producing potentially spectacular results.

A schematic picture of this chain of events is given in Fig. 1. A number of processes must be evaluated to determine the resulting signal. For the specific case of dark photons, it is tempting to simplify the analysis by making a number of assumptions. For example, one may assume that the dark matter capture and annihilation processes have reached equilibrium in the Earth and that the capture cross section has some fixed value, such as the maximal value consistent with current direct detection bounds. Alternatively, the calculations simplify immensely for dark matter masses large compared to all relevant nuclear masses, $m_X \gg m_N$, or dark photon masses $m_{A'}$ large compared to the characteristic momentum transfer so that the interaction is point-like. We show that none of these assumptions are valid in the regions of parameter space of greatest interest; the large m_X approximation may lead to errors of an order of magnitude for $m_X \approx 100$ GeV, and the large $m_{A'}$ approximation may also lead to mis-estimates of factors of a few for very light $m_{A'} \sim$ MeV. To accurately determine the sensitivity of experiments to probe the relevant parameter space, we carry out a general analysis, without making these simplifying assumptions. An early exploration of dark matter accumulation on the Earth mediated by massless dark photons is Ref. [4]. For previous work exploring the case of massive dark photons,
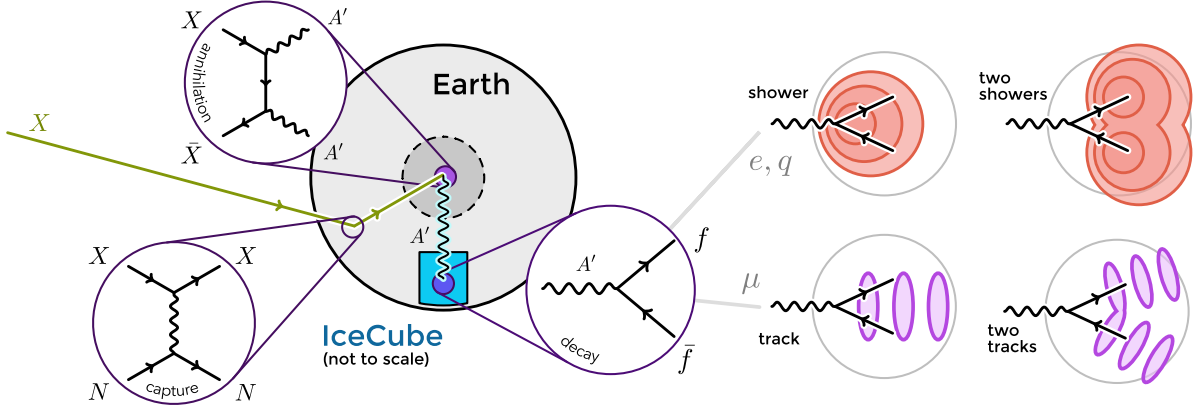
FIG. 1: Dark matter is captured by elastic $XN \to XN$ scattering off nuclei, collects in the center of the Earth, and annihilates to dark photons, $XX \to A'A'$. These dark photons then travel to near the surface of the Earth and decay to SM particles, which may be detected by a variety of experiments, including neutrino telescopes and space-based cosmic ray detectors. As an example, we show IceCube and various signatures there resulting from A' decays to electrons, muons, and hadrons. We discuss the possibility that double tracks (showers) may be resolved spatially (temporally) in the detector.

These results are timely for several reasons. Dark photons have attracted significant interest and are probed in many ways, including direct detection experiments, accelerator and beam dump experiments, and astrophysical observables [5, 6]. The signals we discuss are detectable for dark photon masses $m_{A'} \sim \mathrm{MeV} - \mathrm{GeV}$ and mixing parameters $\varepsilon \sim 10^{-9} - 10^{-7}$, an interesting and large region of parameter space that includes territory that has not yet been probed. These values of $m_{A'}$ can also produce dark matter self-interactions that have been suggested to solve small-scale structure anomalies [35–39]. The range of ε values are naturally induced, for example, by degenerate bi-fundamentals in grand unified theories [40]. It was recently pointed out that combining kinetic mixings of this size with the self-interacting models for small-scale structure can also explain the excess of gamma rays from the galactic center recently observed by Fermi-LAT [41].

At the same time, this work motivates a new class of searches for current indirect detection experiments to discover dark matter. At present there are a number of landmark experiments, including those mentioned above, that are transforming the field of indirect detection with high precision measurements and increasingly large statistics. In many cases, however, their sensitivities for dark matter searches are clouded by uncertainties in astrophysical backgrounds. The signals we highlight here come from a specific direction (the center of the Earth), cannot be mimicked by astrophysics and, in many cases, are essentially background-free. As a result, the processes discussed here provide an opportunity for both current and future experiments to detect a smoking-gun signal of dark matter.

II. DARK PHOTONS

We consider the simplest model of dark matter interacting through dark photons. The low-energy Lagrangian is

$$\mathcal{L} = -\frac{1}{4}\widetilde{F}_{\mu\nu}\widetilde{F}^{\mu\nu} - \frac{1}{4}\widetilde{F}'_{\mu\nu}\widetilde{F}'^{\mu\nu} + \frac{\epsilon}{2}\widetilde{F}_{\mu\nu}\widetilde{F}'^{\mu\nu} - m^2_{\widetilde{A}'}\widetilde{A}'^2$$
$$+ \sum_f \bar{f}(i\slashed{\partial} - q_f e\widetilde{\slashed{A}} - m_f)f + \bar{X}(i\slashed{\partial} - g_X\widetilde{\slashed{A}}' - m_X)X \ , \tag{1}$$

where X is the Dirac fermion dark matter, and $\widetilde{A}$ and $\widetilde{A}'$ are the SM and dark sector gauge fields with field strengths $\widetilde{F}$ and $\widetilde{F}'$ and fine-structure constants $\alpha = e^2/(4\pi)$ and $\alpha_X = g_X^2/(4\pi)$, respectively. The sum is over SM fermions f with SM electric charges q_f. Dark electromagnetism is broken and the mass $m_{\widetilde{A}'}$ is generated by some mechanism, such as the Higgs or Stueckelberg mechanisms, which assume otherwise plays a negligible role in the signals discussed here. Note that the dark matter particles X are stabilized not by some *ad hoc* discrete parity symmetry or even by dark charge conservation (which is broken), but by Lorentz symmetry, since X is the lightest fermion in the dark sector.

After diagonalizing the gauge kinetic and mass terms, the physical states are the usual massless photon A, which does not couple to X, and the dark photon A' with mass $m_{A'} = m_{\widetilde{A}'}/\sqrt{1-\epsilon^2}$, which couples both to X and to SM fermions with charge $\varepsilon q_f e$, where $\varepsilon \equiv \epsilon/\sqrt{1-\epsilon^2}$. We take the independent parameters of the theory to be

$$m_X \ , \ m_{A'} \ , \ \varepsilon \ , \ \alpha_X \ . \tag{2}$$

We typically fix α_X by requiring X to saturate the observed dark matter density through thermal freeze out, so $\alpha_X = \alpha_X^{\text{th}} \simeq 0.035(m_X/\text{TeV})$. Alternatively, the maximum allowed coupling is set by bounds on distortions to the cosmic microwave background [42–44]. Fitting the results from Ref. [45], we find $\alpha_X^{\text{max}} \simeq 0.17(m_X/\text{TeV})^{1.61}$. With a choice of α_X the model is completely determined by the first 3 parameters.

Dark photons decay to SM fermions with width

$$\Gamma(A' \to f\bar{f}) = \frac{N_C\varepsilon^2 q_f^2 \alpha(m_{A'}^2 + 2m_f^2)}{3m_{A'}}\sqrt{1 - \frac{4m_f^2}{m_{A'}^2}} \ , \tag{3}$$

where N_C is the number of colors of fermion f. The dark photons we consider are produced from the annihilation of extremely non-relativistic X particles, and so have energy m_X. For $m_{A'} \gg m_e$, the dark photon decay length is therefore

$$L = R_\oplus B_e \left(\frac{3.6 \times 10^{-9}}{\varepsilon}\right)^2 \left(\frac{m_X/m_{A'}}{1000}\right)\left(\frac{\text{GeV}}{m_{A'}}\right) , \tag{4}$$

where $R_\oplus \simeq 6370$ km is the radius of the Earth, and $B_e \equiv B(A' \to e^+e^-)$ is the branching fraction to electrons. The A' branching fractions can be determined from hadron production at e^+e^- colliders [46]. For $m_{A'} < 2m_\mu$, $B_e = 100\%$. As $m_{A'}$ increases above $2m_\mu$, the $A' \to \mu^+\mu^-$ decay mode opens up rapidly, and B_e drops to 50% at $m_{A'} \sim 300$ MeV. For $500 \text{ MeV} \lesssim m_{A'} \lesssim 3$ GeV, B_e and B_μ are nearly identical and typically vary between 15% and 40%, with the rest made up by decays to hadrons, which also produce photons and neutrinos from meson decays. For m_X at the weak-scale and $m_{A'} \sim 100$ MeV $-$ GeV, the requirement $L \sim R_\oplus$ implies $\varepsilon \sim 10^{-9} - 10^{-7}$, and we will see that this is indeed the range of kinetic mixing parameters that gives the most promising signals.

4

III. DARK MATTER ACCUMULATION IN THE EARTH

Dark matter interacting through dark photons is captured and annihilates at the center of the Earth. The number N_X of dark matter particles in the Earth obeys the equation

$$\frac{dN_X}{dt} = C_{\text{cap}} - C_{\text{ann}}N_X^2 \ , \tag{5}$$

where C_{cap} and $\Gamma_{\text{ann}} = \frac{1}{2}C_{\text{ann}}N_X^2$ are the rates for the capture and annihilation processes. We ignore dark matter evaporation, which is negligible for weak-scale dark matter masses [11, 12]. We also ignore self-capture from dark matter–dark matter self-interactions. The impact of self-capture for the Earth is suppressed by the fact that the escape velocity is low compared to typical galactic dark matter velocities, and so typical dark matter self-scatterings simply replace one captured dark matter particle with another [47].

The solution to Eq. (5) is

$$\Gamma_{\text{ann}} = \frac{1}{2}C_{\text{cap}}\tanh^2\left(\frac{\tau_{\oplus}}{\tau}\right) \ , \tag{6}$$

where $\tau_{\oplus} \simeq 4.5$ Gyr is the age of the Earth, and $\tau = (C_{\text{cap}}C_{\text{ann}})^{-1/2}$ is the timescale for the competing processes of capture and annihilation to reach equilibrium. To evaluate Γ_{ann}, we must therefore evaluate both C_{cap} and C_{ann}, which we now do in turn.

A. Dark Matter Capture

Dark matter particles are captured when elastic scattering off nuclei N in the Earth reduces their velocity below the escape velocity. The elastic scattering process $XN \to XN$ is mediated by t-channel A' exchange. The most relevant scattering targets, N, are iron and nickel; these and other elements are listed in Table I. In the center-of-mass frame, the cross section is

$$\left.\frac{d\sigma_N}{d\Omega}\right|_{\text{CM}} = \frac{1}{(E_X + E_N)^2}\frac{2\varepsilon^2\alpha_X\alpha Z_N^2}{[2\boldsymbol{p}^2(1 - \cos\theta_{\text{CM}}) + m_{A'}^2]^2}|F_N|^2$$
$$\times \left[(E_X E_N + \boldsymbol{p}^2)^2 + (E_X E_N + \boldsymbol{p}^2\cos\theta_{\text{CM}})^2 - (m_X^2 + m_N^2)\boldsymbol{p}^2(1 - \cos\theta_{\text{CM}})\right], \tag{7}$$

where E_N, Z_N, m_N, and F_N are the energy, electric charge, mass, and nuclear form factor of target nucleus N, and $\boldsymbol{p}$ is the center-of-mass 3-momentum of the dark matter. Since the collision is non-relativistic, $\boldsymbol{p}$ is negligible everywhere in Eq. (7), except possibly the denominator. The cross section may then be simplified to

$$\left.\frac{d\sigma_N}{d\Omega}\right|_{\text{CM}} \approx 4\varepsilon^2\alpha_X\alpha Z_N^2\frac{\mu_N^2}{(2\boldsymbol{p}^2(1 - \cos\theta_{\text{CM}}) + m_{A'}^2)^2}|F_N|^2 \ . \tag{8}$$

where $\mu_N \equiv m_N m_X/(m_N + m_X)$ is the reduced mass of the X–N system.

It is tempting to simplify the denominator by neglecting $\boldsymbol{p}$, and reducing the A' exchange to a contact interaction. However, it is not always true that $m_{A'}^2 \gg \boldsymbol{p}^2$ so that the latter term may be neglected. The typical size of the momentum is $\boldsymbol{p}^2 \sim \mu_N^2 w^2$, where w is the X velocity in the lab frame. Since capture typically occurs only for very small asymptotic dark matter velocities, a reasonable choice would be $w = v_{\oplus}(r_N) \approx 5 \times 10^{-5}$, the escape

velocity at the radius r_N that maximizes the radial number density $n_N(r)r^2$ of target nucleus N. With these values, the contact interaction limit fails for $m_{A'} \lesssim 3$ MeV. Rather than neglecting the momentum term altogether, a slightly more sophisticated approach would be to make the substitution $\boldsymbol{p}^2(1 - \cos\theta_{\mathrm{CM}}) \to \mu_N^2 w^2$. In this work, however, we keep the full $\boldsymbol{p}$ dependence in the propagator and evaluate the capture rate numerically so that our results are valid throughout parameter space. We have confirmed that our results reproduce those in the literature in the corners of parameter space where simplifying assumptions are valid. For example, they match Ref. [48] in the large-$m_{A'}$, point-like cross section limit.

To determine capture rates, it is convenient to re-express the differential cross section as a function of recoil energy $E_R = \mu_N^2 w^2 (1 - \cos\theta_{\mathrm{CM}})/m_N$ in the lab frame. In the non-relativistic limit the expression simplifies to [49]

$$\frac{d\sigma_N}{dE_R} \approx 8\pi\varepsilon^2\alpha_X\alpha Z_N^2 \frac{m_N}{w^2(2m_N E_R + m_{A'}^2)^2}|F_N|^2 \ . \tag{9}$$

For F_N, we adopt the Helm form factor [50],

$$|F_N(E_R)|^2 = \exp\left[-E_R/E_N\right] \ , \tag{10}$$

where $E_N \equiv 0.114\ \mathrm{GeV}/A_N^{5/3}$ is a characteristic energy scale for a target nucleus with atomic mass number A_N.

From this fundamental cross section we can determine the capture rate. The differential rate of dark matter particles scattering off nuclei with incident velocity w at radius r from the center of the Earth and imparting recoil energy between E_R and $E_R + dE_R$ is given by

$$dC_{\mathrm{cap}} = n_X \sum_N n_N(r) \frac{d\sigma_N}{dE_R} w\, f_\oplus(w,r)\, d^3w\, d^3r\, dE_R \ , \tag{11}$$

where $n_X = (0.3\ \mathrm{GeV/cm^3})/m_X$ and $n_N(r)$ are the dark matter and target nucleus number densities, respectively, and $f_\oplus(w,r)$ is the velocity distribution of incident dark matter at radius r, which is distorted from the free-space Maxwell–Boltzmann distribution, $f(u)$, by the Earth's motion and gravitational potential. We follow the velocity notation introduced by Gould [13, 14, 16] where $v_\oplus(r)$ is the escape velocity at radius r and u is the dark matter velocity asymptotically far from the Earth.

The total capture rate is obtained by integrating Eq. (11) over the region of parameter space where the final state dark matter particle has energy less than $m_X v_\oplus^2(r)/2$ and is thus gravitationally captured. The escape velocity $v_\oplus(r)$ and number densities $n_N(r)$ are determined straightforwardly from the density data enumerated in the Preliminary Reference Earth Model [51]. Following Edsjö and Lundberg [20], the target number densities are modeled by dividing the Earth into two layers, the core and the mantle, with constant densities and elemental compositions given in Table I. The capture rate is then $C_{\mathrm{cap}} = \sum_N C_{\mathrm{cap}}^N$, where the rate on target N is

$$C_{\mathrm{cap}}^N = n_X \int_0^{R_\oplus} dr\, 4\pi r^2 n_N(r) \int_0^\infty dw\, 4\pi w^3 f_\oplus(w,r) \int_{E_{\mathrm{min}}}^{E_{\mathrm{max}}} dE_R \frac{d\sigma_N}{dE_R}\, \Theta(\Delta E) \ . \tag{12}$$

Here $\Theta(\Delta E) = \Theta(E_{\mathrm{max}} - E_{\mathrm{min}})$ imposes the constraint that capture is kinematically possible by enforcing that the minimum energy transfer, E_{min}, to gravitationally capture the dark

6

Element	Core MF	Mantle MF	$C_{\rm cap}^N({\rm s}^{-1})$	Element	Core MF	Mantle MF	$C_{\rm cap}^N({\rm s}^{-1})$
Iron	0.855	0.0626	9.43×10^7	Chromium	0.009	0.0026	8.98×10^5
Nickel	0.052	0.00196	7.10×10^6	Oxygen	0	0.440	4.03×10^5
Silicon	0.06	0.210	2.24×10^6	Sulfur	0.019	0.00025	2.41×10^5
Magnesium	0	0.228	1.05×10^6	Aluminum	0	0.0235	1.62×10^5
Calcium	0	0.0253	9.06×10^5	Phosphorus	0.002	0.00009	2.04×10^4

TABLE I: Mass fractions of the Earth's core and mantle for the elements most relevant for dark matter capture [20, 52]. Also shown for each element is the capture rate $C_{\rm cap}^N$ for $m_X = 1$ TeV, $m_{A'} = 1$ GeV, $\varepsilon = 10^{-8}$, and $\alpha_X = \alpha_X^{\rm th} \simeq 0.035$ as a measure of the relevance of the nuclear target for dark matter capture.

matter particle is smaller than the maximum recoil energy kinematically allowed, $E_{\rm max}$, corresponding to $\cos\theta_{\rm CM} = -1$. Explicitly, these energies are

$$E_{\rm min} = \frac{1}{2}m_X \left[w^2 - v_\oplus^2(r)\right] \qquad\qquad E_{\rm max} = \frac{2\mu_N^2}{m_N}w^2 \ . \tag{13}$$

To make further progress, we must determine the distribution $f_\oplus(w, r)$. A simple approach is to only include the effect of the Earth's gravitational potential. However, the Earth is within the gravitational influence of the Sun, and one might expect the acceleration of dark matter by the sun to suppress or eliminate the capture of heavy dark matter particles by the Earth. In 1991, however, Gould argued that the interactions of dark matter with other planets leads to diffusion of the dark matter population between bound and unbound orbits and one could thus ignore the impact of the Sun's gravitational field and treat the Earth in the "free-space" approximation to reasonable accuracy [53].

More recently, however, this simple picture has been refined with both potentially positive and negative implications. In numerical work, both Lundberg and Edsjö [20] and Peter [21–23] have investigated the influence of the Sun, Earth, Jupiter, and Venus in more detail, tracking the possibility that the Earth's dark matter population is suppressed when particles are kicked out of the solar system or captured by the Sun. For the case of supersymmetric WIMPs—that is, dark matter with weak-scale mediators—they have found that these effects can reduce the Earth's capture rate by one order of magnitude or more, depending on the dark matter mass. On the other hand, simulations of galaxies with baryons have shown that dark matter substructures may be pulled into the disk and create a significant and relatively cold enhancement of the local dark matter density known as a "dark disk" [54, 55]. For the case of WIMP dark matter, this population may enhance indirect detection signals from the Earth by up to three orders of magnitude [24, 56]. Note that the dark disk has a velocity relative to our solar system that is $\sim 1/5$ that of the ordinary dark matter halo [57]. It is thus plausible that the dark disk populates a region in phase space more amenable to Earth capture without significantly enhancing the direct detection rate.

As we show below, the dark photon case differs significantly from WIMPs, because both the capture and annihilation rates are highly velocity dependent. One consequence of this is that $\tau_\oplus$ is typically larger than τ in Eq. (6), as opposed to the conventional wisdom that the Earth has not reached its WIMP capacity. It is therefore not possible to simply extrapolate the conclusions of WIMP studies to the present framework. In addition, as our analysis is valid for general dark matter and dark photon masses, inaccuracies in the particle physics

modeling are greatly reduced, and the astrophysical uncertainties from dark disk and other effects are very likely the dominant uncertainties entering the signal rate derivation. These astrophysical phenomena are therefore clearly interesting and important, but are beyond the scope of the present work. Here, we use the free-space approximation, not because it is the last word, but because it provides a simple "middle ground" estimate, with both suppressions and enhancements possible.

With the free-space assumption, we proceed as follows. By energy conservation, w and u, the incident dark matter particle's velocities in the Earth's and galactic frame, respectively, are related by

$$w^2 = u^2 + v_\oplus^2(r) \ . \tag{14}$$

The capture rate for a general $d\sigma_N/dE_R$ can then be rewritten as

$$C_{\text{cap}}^N = n_X \int_0^{R_\oplus} dr \, 4\pi r^2 n_N(r) \int_0^\infty du \, 4\pi u^2 f_\oplus(u) \frac{u^2 + v_\oplus^2(r)}{u} \int_{E_{\text{min}}}^{E_{\text{max}}} dE_R \frac{d\sigma_N}{dE_R} \, \Theta(\Delta E) \ . \tag{15}$$

Here $f_\oplus(u)$ is defined to be the angular-averaged and annual-averaged velocity distribution in the rest frame of the Earth [58],

$$f_\oplus(u) = \frac{1}{4} \iint_{-1}^1 d\cos\theta \, d\cos\phi \, f\left[\left(u^2 + (V_\odot + V_\oplus \cos\phi)^2 + 2u(V_\odot + V_\oplus \cos\phi)\cos\theta\right)^{1/2}\right] , \tag{16}$$

where $V_\odot \simeq 220$ km/s is the velocity of the Sun relative to the galactic center, and $V_\oplus \simeq 29.8$ km/s is the velocity of the Earth relative to the Sun. Many-body simulations and other considerations suggest a dark matter velocity distribution in the galactic rest frame of the form [59–64]

$$f(u) = N_0 \left[\exp\left(\frac{v_{\text{gal}}^2 - u^2}{k u_0^2}\right) - 1\right]^k \Theta(v_{\text{gal}} - u) \ , \tag{17}$$

where N_0 is a normalization constant, v_{gal} is the escape velocity from the galaxy, and the parameters describing the distribution have typical values in the ranges [48, 65]

$$220 \text{ km/s} < u_0 < 270 \text{ km/s} \qquad 450 \text{ km/s} < v_{\text{gal}} < 650 \text{ km/s} \qquad 1.5 < k < 3.5 \ . \tag{18}$$

We use the midpoint values of each of these, namely, $u_0 = 245$ km/s, $v_{\text{gal}} = 550$ km/s, and $k = 2.5$. The truncated Maxwell–Boltzmann distribution is recovered for $k = 0$.

Upon inserting Eq. (9), the dE_R integral in Eq. (15) evaluates to

$$\int_{E_{\text{min}}}^{E_{\text{max}}} dE_R \frac{d\sigma_N}{dE_R} = \frac{2\pi\varepsilon^2 \alpha_X \alpha Z_N^2}{w^2 m_N E_N} e^{\frac{m_{A'}^2}{2m_N E_N}} \left[\frac{e^{-x_N}}{x_N} + \text{Ei}(-x_N)\right]_{x_N^{\text{max}}}^{x_N^{\text{min}}} , \tag{19}$$

where we use the substitution variable x_N and exponential integral function [66],

$$x_N = \frac{2m_N E_R + m_{A'}^2}{2m_N E_N} \qquad\qquad \text{Ei}(z) \equiv -\int_{-z}^\infty dt \frac{e^{-t}}{t} \ . \tag{20}$$

The total rate is $C_{\text{cap}} = \sum C_{\text{cap}}^N = 32\pi^3 \varepsilon^2 \alpha_X \alpha n_X \sum_N Z_N^2 (m_N E_N)^{-1} \exp\left(\frac{m_{A'}^2}{2m_N E_N}\right) c_{\text{cap}}^N$, where

$$c_{\text{cap}}^N = \int_0^{R_\oplus} dr \, r^2 n_N(r) \int_0^\infty du \, u f_\oplus(u) \Theta(\Delta x_N) \left[\frac{e^{-x_N}}{x_N} + \text{Ei}(-x_N)\right]_{x_N^{\text{max}}}^{x_N^{\text{min}}} . \tag{21}$$

The capture rates C_{cap}^N for various nuclei N at a representative point in parameter space are shown in Table I.

8

B. Dark Matter Annihilation

Once a dark matter particle is captured by the Earth, it repeatedly re-scatters, drops to the center of the Earth, and eventually thermalizes with the surrounding matter. In the case of the Sun, the dark matter thermalizes within the age of the Sun for X–proton spin-independent scattering cross sections greater than 10^{-51}, 10^{-50}, and 10^{-47} cm^2 for $m_X = 100$ GeV, 1 TeV, and 10 TeV, respectively [23]. Similar studies of Earth capture are not available. However, we will find that, for the range of parameters where an observable indirect signal is possible, the direct detection X–proton cross sections are at least $\sigma_p \sim 10^{-48}$ cm^2, corresponding to X–iron cross sections of $\sigma_{\mathrm{Fe}} \sim Z_{\mathrm{Fe}}^2 (m_{\mathrm{Fe}}/m_p)^2 \sigma_p \sim 10^{-42}$ cm^2, many orders of magnitude larger than required for thermalization in the Sun. We therefore expect dark matter to be thermalized in the Earth to an excellent approximation.

For thermalized dark matter, the annihilation rate parameter C_{ann} is [48]

$$C_{\mathrm{ann}} = \langle \sigma_{\mathrm{ann}} v \rangle \left[\frac{G_N m_X \rho_\oplus}{3 T_\oplus} \right]^{3/2} , \tag{22}$$

where $\rho_\oplus \approx 13$ g/cm^3 and $T_\oplus \approx 5700$ K are the matter density and temperature at the center of the Earth, respectively, σ_{ann} is the cross section for $XX \to A'A'$, and v is the relative velocity of the interacting particles, which is double the velocity of either interacting particle in the center-of-mass frame.

The thermally-averaged cross section is

$$\langle \sigma_{\mathrm{ann}} v \rangle = (\sigma_{\mathrm{ann}} v)_{\mathrm{tree}} \langle S_S \rangle , \tag{23}$$

where

$$(\sigma_{\mathrm{ann}} v)_{\mathrm{tree}} = \frac{\pi \alpha_X^2}{m_X^2} \frac{[1 - m_{A'}^2/m_X^2]^{3/2}}{[1 - m_{A'}^2/(2m_X^2)]^2} \tag{24}$$

is the tree-level cross section [67], and $\langle S_S \rangle$ is the thermal average of the S-wave Sommerfeld enhancement factor. This Sommerfeld enhancement factor [68] has been determined with various degrees of refinement. An analytic expression that includes the resonance behavior present for non-zero $m_{A'}$ can be derived by approximating the Yukawa potential by the Hulthén potential [69–71]. The resulting Sommerfeld factor is

$$S_S = \frac{\pi}{a} \frac{\sinh(2\pi a c)}{\cosh(2\pi a c) - \cos(2\pi \sqrt{c - a^2 c^2})} , \tag{25}$$

where $a = v/(2\alpha_X)$ and $c = 6\alpha_X m_X/(\pi^2 m_{A'})$. The thermal average is, then,

$$\langle S_S \rangle = \int \frac{d^3 v}{(2\pi v_0^2)^{3/2}} e^{-\frac{1}{2} v^2/v_0^2} S_S , \tag{26}$$

where $v_0 = \sqrt{2 T_\oplus/m_X}$.

C. Equilibrium Time Scales

In Fig. 2 we present results for the equilibrium timescale $\tau = (C_{\mathrm{cap}} C_{\mathrm{ann}})^{-1/2}$ in the $(m_{A'}, \varepsilon)$ plane for $m_X = 100$ GeV without Sommerfeld enhancement, and $m_X =$
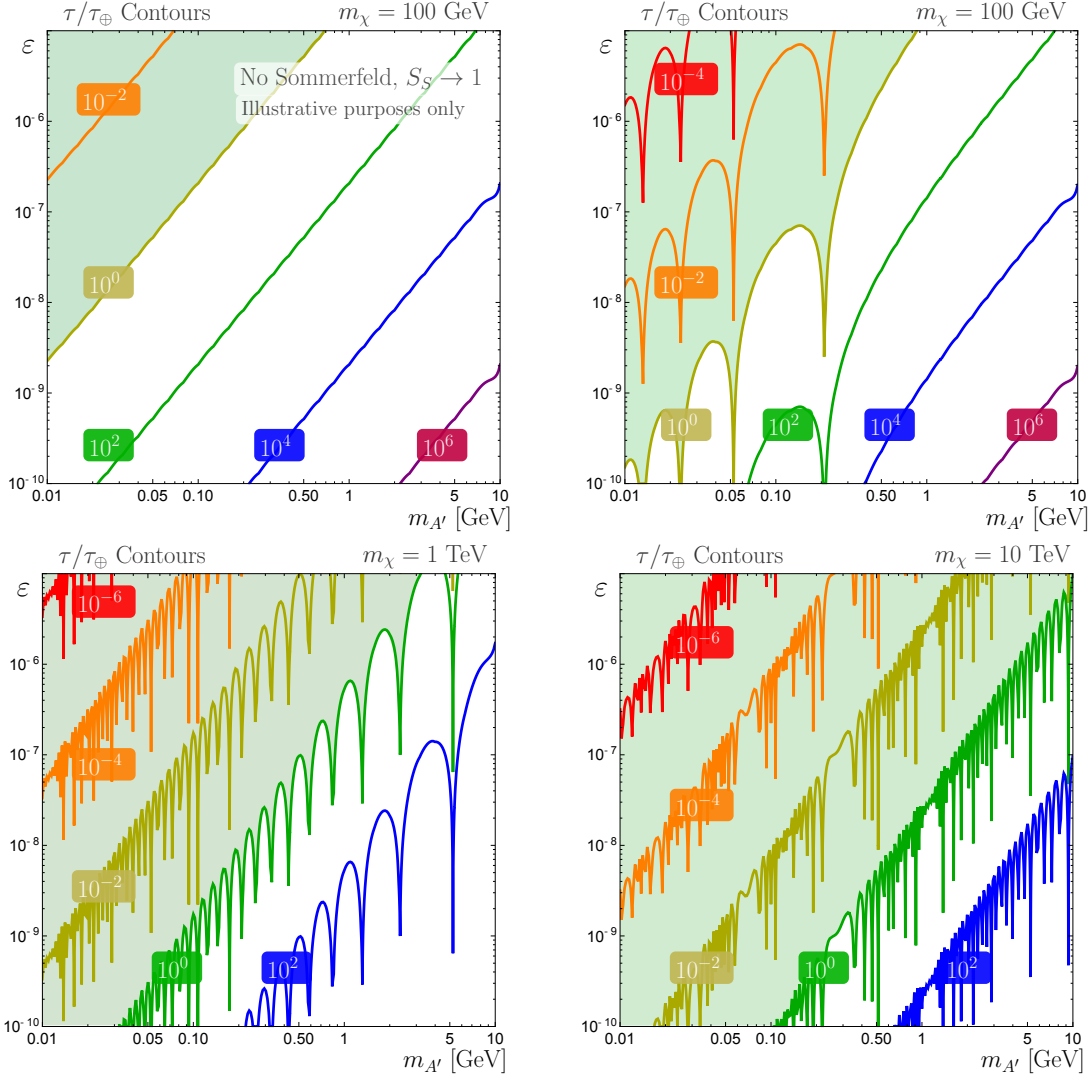
FIG. 2: Contours of constant $\tau/\tau_\oplus$, the equilibrium timescale in units of the Earth's lifetime, in the $(m_{A'}, \varepsilon)$ plane for $m_X = 100$ GeV without (top left) and with (top right) the Sommerfeld enhancement factor, $m_X = 1$ TeV with the Sommerfeld factor (bottom left), and $m_X = 10$ TeV with the Sommerfeld factor (bottom right). The dark sector fine-structure constant α_X is set by requiring $\Omega_X \simeq 0.23$. In the green shaded regions, the Earth's lifetime is greater than the equilibrium timescale, $\tau_\oplus > \tau$.

100 GeV, 1 TeV, 10 TeV with Sommerfeld enhancement. The dark coupling α_X is fixed by the thermal relic density. For $m_{A'} \ll m_X$, the parametric dependence of τ on ε and $m_{A'}$ enters dominantly through C_{ann} and is $\tau \sim C_{\mathrm{ann}}^{-1/2} \sim m_{A'}^2/\varepsilon$. This can be seen in the baseline values of the contours in Fig. 2. The bumps in the contours reflect the resonance structure of the Sommerfeld enhancement factor $\langle S_S \rangle$.

In the shaded green (upper left) parts of the figures, the Earth's dark matter population has reached its maximal (equilibrium) value, and so the annihilation rate is essentially determined by the capture rate, with $\Gamma_{\mathrm{ann}} \approx \frac{1}{2} C_{\mathrm{cap}}$. As one moves down and to the right, however, the equilibrium timescale grows, and the population is eventually not maximal. We will see that when the population is not at its maximal value, the signal quickly becomes

10

undetectable.

The Sommerfeld enhancement plays an essential role in reducing the equilibrium timescale and making the signal detectable in large regions of the $(m_{A'}, \varepsilon)$ plane. For capture, the typical velocity that enters has an irreducible contribution from the gravitational potential that accelerates dark matter as it falls into the Earth. Capture interactions, therefore, occur at the typical escape velocity in the Earth's core, $v_{\text{esc}} \approx 5.0 \times 10^{-5}$. However, after the dark matter particles are captured, they sink to the core, and come into thermal equilibrium with the normal matter. As a result, the population of dark matter particles at the center of the Earth is even colder, with relative velocities $v_0 \approx 1.0 \times 10^{-6} \, [\text{TeV}/m_X]^{1/2}$. In the $m_{A'} \ll \alpha_X m_X$ limit, the Sommerfeld factor of Eq. (25) becomes

$$S_0 = \frac{2\pi \, \alpha_X/v}{1 - e^{-2\pi\alpha_X/v}} \ . \tag{27}$$

For thermal relics, S_0 is therefore typically $\sim 2\pi\alpha_X/v \sim 10^4 - 10^6$. Sommerfeld enhancement therefore reduces the equilibrium timescale by factors of ~ 100 for $m_X \sim 100$ GeV, as can be seen in Fig. 2 by comparing the top right and top left panels. This reduction on τ goes to ~ 1000 for $m_X \sim 10$ TeV. The Sommerfeld factor therefore plays an essential role in boosting the current Earth's dark matter population and the dark matter signal [26].

IV.   SIGNAL RATES AND CHARACTERISTICS

After dark matter accumulates in the center of the Earth and annihilates to dark photons, the dark photons propagate outwards with essentially no interactions with matter. The characteristic radius of the thermalized dark matter distribution in the Earth is [48]

$$r_X = \left(\frac{3T_\oplus}{2\pi G_N \rho_\oplus m_X} \right)^{1/2} \approx 150 \text{ km} \sqrt{\frac{\text{TeV}}{m_X}} \ . \tag{28}$$

An observer at the surface of the Earth or in low Earth orbit therefore sees the majority of dark matter annihilations take place within $1.3° \sqrt{\text{TeV}/m_X}$ of straight down.

The dark photons are highly boosted with energy m_X. In the decay $A' \to f\bar{f}$, the characteristic angle between the direction of a parent A' and its decay products in the Earth's rest frame is

$$\theta \sim \tan^{-1} \left(\frac{m_{A'}^2 - 4m_f^2}{m_X^2 - m_{A'}^2} \right)^{1/2} \approx \frac{\sqrt{m_{A'}^2 - 4m_f^2}}{m_X} \ , \tag{29}$$

assuming $m_{A'} \ll m_X$. Much larger opening angles are possible, however, as discussed in detail in the Appendix.

The indirect detection signal is therefore two highly collimated leptons or jets that point back to the center of the Earth within a few degrees. As we will discuss, in some cases, the two leptons or jets may be simultaneously detected, and possibly even seen as two different particles, in contrast to the standard neutrino-based indirect detection signals, where there is only one primary particle. In any case, the signal of high-energy particles from the center of the Earth distinguishes the signal from all possible astrophysical backgrounds, potentially providing a smoking-gun signal of dark matter if the event rates are large enough.

We now determine the event rates and characteristics for two classes of experiments: under-ice/underground/underwater detectors, represented by IceCube, and space-based experiments, represented by Fermi-LAT and AMS-02.

A. IceCube

Dark photons may be detected in IceCube if they decay in IceCube or just below it. Decays $A' \to e^+ e^-, q\bar{q}$ will be seen as showers, and for $m_{A'} \gtrsim 300$ MeV, typically 15% – 40% of the decays will be to muons [46] and be seen as tracks. The number of dark photon decays that can be detected by IceCube is

$$N_{\text{sig}} = 2\,\Gamma_{\text{ann}}\,\frac{A_{\text{eff}}}{4\pi R_{\oplus}^2}\,\epsilon_{\text{decay}}\,T\ , \tag{30}$$

where the factor of 2 results from the fact that each annihilation produces two dark photons, A_{eff} is the effective area of detector,

$$\epsilon_{\text{decay}} = e^{-R_{\oplus}/L} - e^{-(R_{\oplus}+D)/L} \tag{31}$$

is the probability that the dark photon decays after traveling a distance between $R_{\oplus}$ and $R_{\oplus} + D$, where D is the effective depth of the detector, and T is the live time of the experiment.

To very roughly estimate the detection rates for IceCube, we expect that for $m_X \sim 1$ TeV, all dark photons that decay within the instrumented volume of IceCube are detected, and so we take $A_{\text{eff}} \approx 1$ km^2 and $D \approx 1$ km. For lighter dark matter, say, $m_X \sim 100$ GeV, the decay products may be lost between the photomultiplier strings of IceCube. But these should be seen with high efficiency in DeepCore [72], the subset of IceCube with finer string spacings and lower threshold, and so we also present results for the instrumented volume of DeepCore, with $A_{\text{eff}} \approx 0.067$ km^2 and $D \approx 0.55$ km.

In Fig. 3 we present the number of signal events for $m_X = 100$ GeV, 1 TeV, and 10 TeV in the $(m_{A'}, \varepsilon)$ plane. The bumpy features and closed contours are real physical features resulting from Sommerfeld enhancement resonances. Also shown are the regions of parameter space disfavored by existing bounds on dark-photon-mediated $XN \to XN$ scattering from direct detection experiments, such as XENON100 and LUX [73], and X-independent bounds on dark photons from beam dump experiments and supernovae [5, 74–77]. We use the recently updated supernova cooling bounds in Ref. [77] which differ from earlier calculations for emission of light particles by including multiple pion exchange processes. As a result, these cooling bounds are about an order of magnitude weaker than previous limits based on single pion exchange.

We see that the indirect detection signal discussed here probes regions of parameter space that are so far inaccessible by other methods. As anticipated in Sec. II, the indirect detection signal is largest for $\varepsilon \sim 10^{-9} - 10^{-7}$, where the A' decay length is comparable to $R_{\oplus}$. For $m_X \sim$ TeV and $\varepsilon \sim 10^{-8}$, for example, $N_{\text{sig}} \sim 10,000$ events over 10 years are possible in regions of parameter space that are otherwise currently viable. IceCube has collected roughly 7 years of data already, and so detailed analyses will either exclude large new regions of the $(m_{A'}, \varepsilon)$ parameter space or discover dark matter.

For $m_X \sim 100$ GeV, the indirect and direct detection sensitivities are comparable for α_X between α_X^{th} and α_X^{max}. The indirect and direct detection sensitivities are shown in the conventional (m_X, σ_{Xn}) plane in Fig. 4, where σ_{Xn} is the spin-independent X–nucleon cross section: $\mu_T^2 A_T^2 \sigma_{Xn} = \mu_n^2 \sigma_{XT}$ with $T = $ Xe. The indirect detection signal is suppressed for both large σ_{Xn} (large ε, dark photons decay too soon) and small σ_{Xn} (small ε, dark matter capture is too slow and the captive population does not equilibrate). Of course, the large σ_{Xn} are already excluded by direct detection experiments. Focusing on the small σ_{Xn} region, for
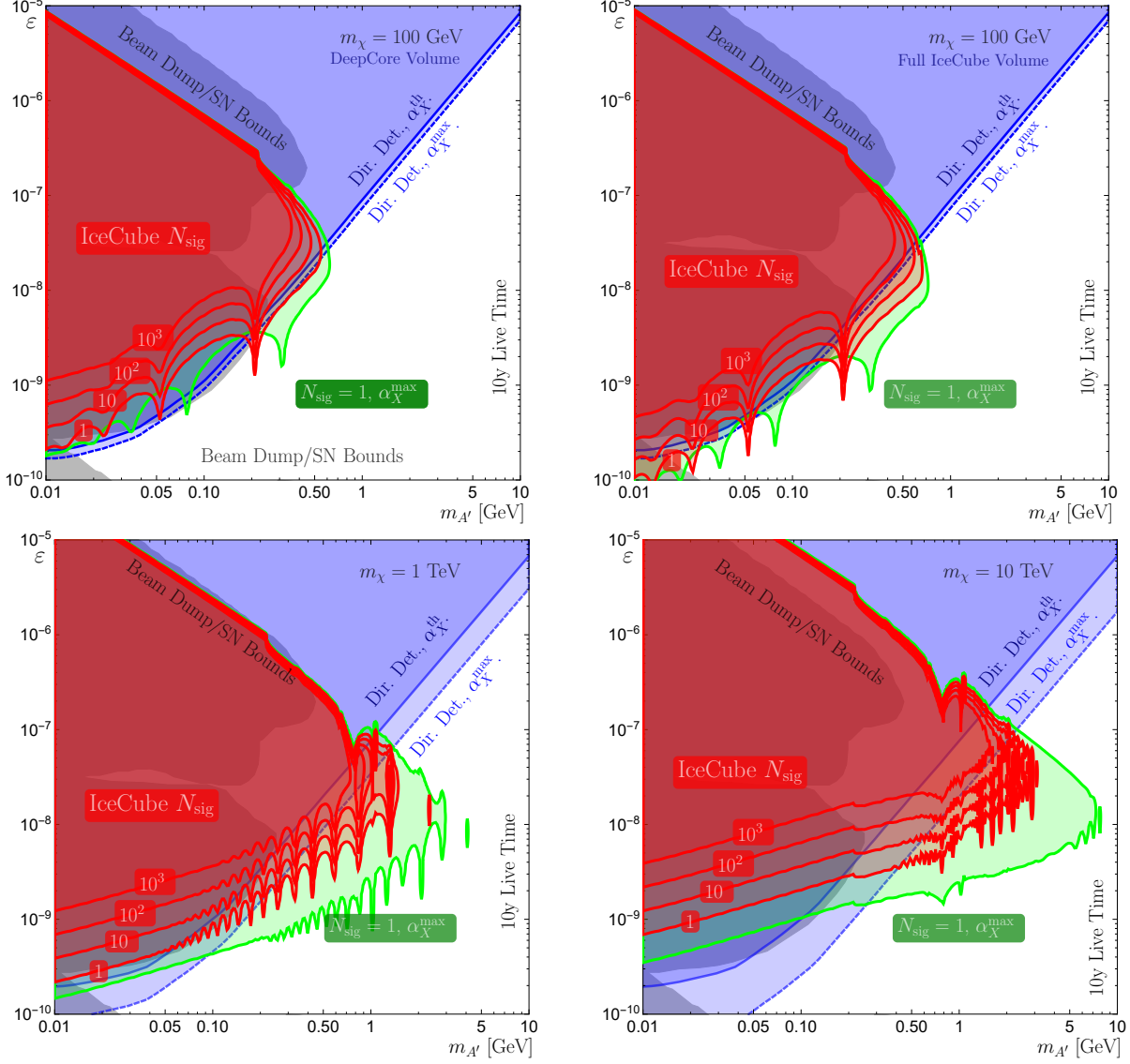
FIG. 3: **Red:** IceCube event rates for $T = 10$ years live time in the $(m_{A'}, \varepsilon)$ plane for $m_X = 100$ GeV in DeepCore (top left) and IceCube (top right), $m_X = 1$ TeV in IceCube (bottom left), and $m_X = 10$ TeV in IceCube (bottom right). The dark sector fine-structure constant is set to the value α_X^{th} which realizes $\Omega_X \simeq 0.23$. **Green:** Single event reach for the maximal dark fine-structure constant α_X^{max} allowed by cosmic microwave background distortion bounds [45]. **Blue:** current bounds from direct detection [73]. **Gray:** regions probed by beam dump and supernovae constraints [5, 74–77].

$m_X > 100$ GeV, the indirect detection signals probe cross sections as much as three orders of magnitude below the current bounds from direct detection experiments, such as XENON and LUX.

Since $\sigma_{Xn} \sim \alpha_X \varepsilon^2$, a given σ_{Xn} corresponds to a larger value of ε when assuming the thermal α_X^{th} versus maximal α_X^{max} dark sector coupling. For this reason, the dashed α_X^{max} curves on the left-hand plot in Fig. 4 are sometimes above the solid α_X^{th} curves on the (m_X, σ_{Xn}) plane. This is because when going from α_X^{th} to α_X^{max}, the additional ε reach gained in indirect detection experiments is less than that in direct detection experiments.

13
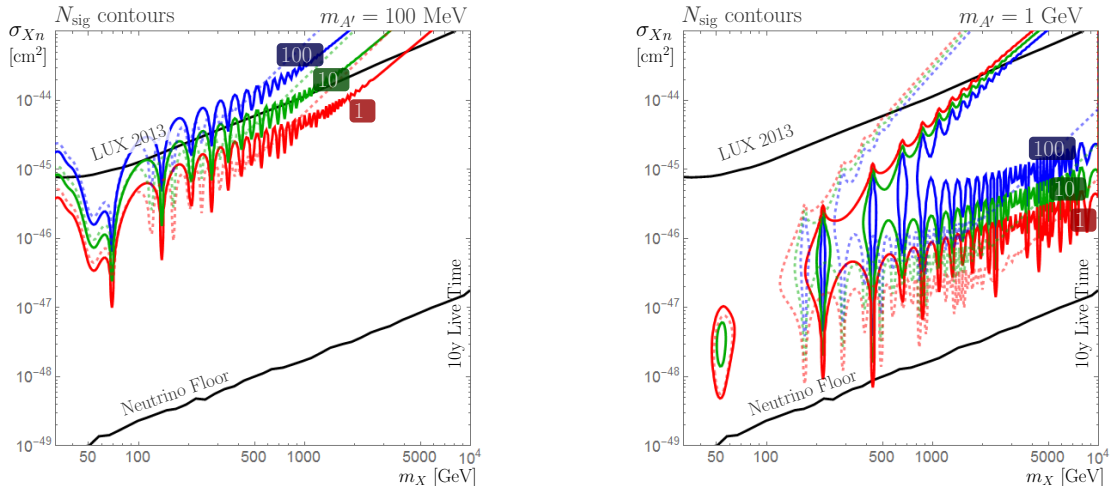
FIG. 4: Comparison of indirect and direct detection sensitivities in the (m_X, σ_{Xn}) plane for $m_{A'} = 100$ MeV (left) and 1 GeV (right). The direct detection bounds are from the LUX collaboration [78]. In this regime the interaction is effective point-like in contrast to the low $m_{A'}$ region [73, 79, 80] in Fig. 3, where the direct detection bounds become independent of $m_{A'}$ for low $m_{A'}$. Also shown is the 'neutrino floor,' where coherent neutrino scattering affects direct detection experiments [81]; the dashed line is an extrapolation.

The reason for this is straightforward: the lower bound on the IceCube reach is set by the condition that the $\tanh^2(\tau_{\oplus}/\tau)$ in Eq. (6) is 'saturated' near unity, i.e. that dark matter capture and annihilation are in equilibrium. This is why the lower contours of Fig. 3 display the same resonances as Fig. 2. Since this condition is set by the geometric mean of the capture and annihilation rates, it scales differently from direct detection experiments which has the same parametric dependence as the capture rate.

For sufficiently small dark matter masses $\alpha_X^{\rm th} > \alpha_X^{\rm max}$; see, for example, the discussion below Eq. (2). This is seen in the right-hand plot of Fig. 4, where the $N_S = 10$ (dashed green) $\alpha_X^{\rm max}$ contour disappears in the low-m_X bubble.

The detector's effective area $A_{\rm eff}$ and depth D are, of course, dependent on the energy and type of the dark photon decay products, and a more detailed study of detector response is required to estimate these more accurately. This is beyond the scope of the present work, but we note here some basic considerations. Muons with energies $E_\mu \sim 100$ GeV $-$ TeV lose energy primarily through ionization and travel a distance

$$L_\mu = \frac{1}{\rho\beta} \ln\left[\frac{\alpha + \beta E_\mu}{\alpha + \beta E_{\rm th}}\right] \tag{32}$$

before their energy drops below a threshold energy $E_{\rm th}$, where $\rho = 1$ g/cm^3, $\alpha \simeq 2.0$ MeV cm^2/g, and $\beta \simeq 4.2 \times 10^{-6}$ cm^2/g [82]. For $E_\mu = 1$ TeV and $E_{\rm th} = 50$ GeV, on average muons travel a distance $L_\mu = 2.5$ km. Dark photons that decay to muons a km or two below IceCube may therefore be detected in IceCube, and so the effective depth of IceCube is a bit larger than 1 km. For $m_X \sim 10$ TeV, the effective depth is larger still, although less than a naive application of Eq. (32) would indicate, as such high energy muons lose energy primarily through radiative processes. At TeV energies, the experimental angular resolution for muon tracks is less than a degree, providing a powerful handle to reduce background. For the case of showers from electrons or hadrons, the angular resolution

14
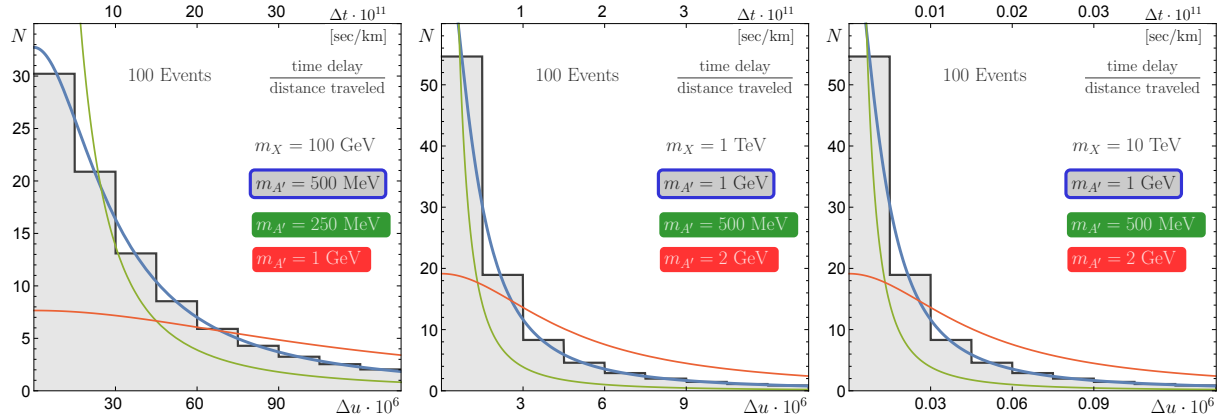
FIG. 5: Lab-frame muon velocity differences for $A' \to \mu^+\mu^-$ and $(m_X, m_{A'}) = (100\,\text{GeV}, 500\,\text{MeV})$ (left), $(1\,\text{TeV}, 1\,\text{GeV})$ (center), and $(10\,\text{TeV}, 1\,\text{GeV})$ (right). Distributions are normalized to 100 events and different values of $m_{A'}$ are shown for comparison. The top axes measure the time delay between the two final states per km between the decay and observation positions.

is worse, but still sufficient to identify showers as up-going to within tens of degrees. In addition, because dark photons decay completely to visible particles, contained events are mono-energetic, with the total energy equal to m_X. The angle and energy distributions of tracks and showers are therefore completely different from astrophysical sources, and provide powerful handles for differentiating signal from background.

The dark photon signal has two primaries, which could in principle be identified as a smoking-gun signal for the dark sector. In Figs. 5 and 6 we show histograms of the velocity difference (time delay) and opening angle (track separation) of the two muons produced in a dark photon decay. Details of the distributions are presented in the Appendix. Parallel tracks have been considered previously in the context of slepton production from high energy neutrinos in Refs. [83, 84] and have recently been searched for by IceCube [85]. As a benchmark for IceCube reach, the parameters $m_X = 1\,\text{TeV}$, $m_{A'} = 1.3\,\text{GeV}$, and $\varepsilon = 2\times10^{-8}$ gives an expected 40 muon events in 10 live years. The center panels of Figs. 5 and 6 then show that over ~ 2.5 km between the A' decay point and the maximal detection distance, one expects a few events with timing separation of ~ 0.03 ns and ~ 20 m track separation.

The timing separation is below the IceCube Digital Optical Module timing resolution of ~ 5 ns [86]. The track separations are less than the ~ 100 m separations probed by current analyses [85], but they are also much larger than the ~ 1 m separations from SM neutrino-induced charm production. These results motivate looking for parallel muon tracks with $\mathcal{O}(10\,\text{m})$ separations, which would be an unambiguous signal of physics beyond the SM, and a spectacular signal of dark photons and dark matter. One step in this direction is the proposed PINGU upgrade which would densely instrument a subset of the IceCube/DeepCore detector [87]. However, for the proposed dark photon search, this comes at a large cost in available volume and propagation distance. A possible alternative direction to improve sensitivity to these parallel muon signals is to increase the detector density of the IceTop surface array.
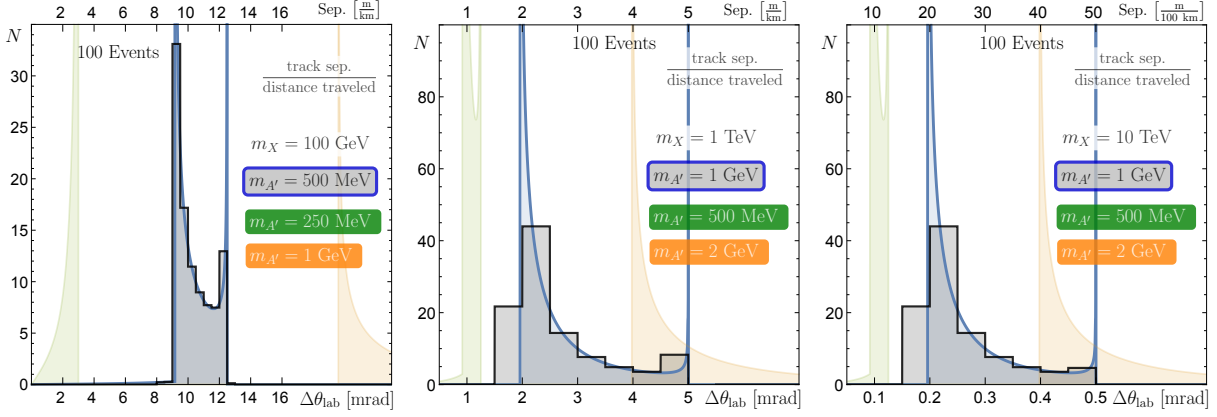
FIG. 6: Lab-frame muon opening angles (bottom axis)/track separation (top axis) for $A' \to \mu^+\mu^-$ and the same m_X values as Fig. 5. Different values of $m_{A'}$ are shown for comparison.
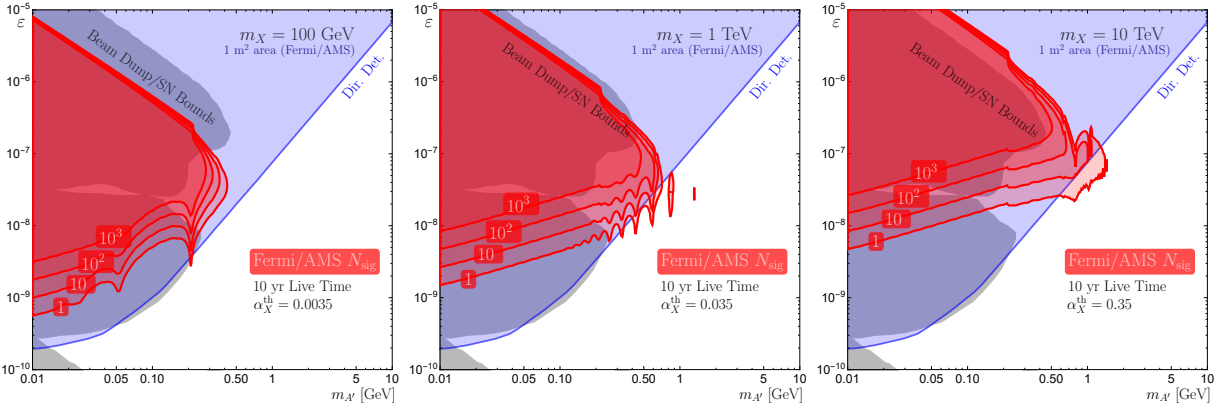
FIG. 7: 10 year signal event rates for a space-based detector in low Earth orbit, such as Fermi/AMS. Colors and bounds are the same as Fig. 3.

B. Fermi-LAT/AMS-02

The dark photon decay products may also be detected by space-based cosmic ray detectors, such as Fermi-LAT and AMS-02. Though these are far smaller than IceCube, the dark photon may decay anywhere between the Earth's surface and the detector, providing a partially-compensating enhancement to the rate. For Fermi and AMS, we follow the formalism described above, but now use $A_{\mathrm{eff}} = 1$ m^2. Both Fermi and AMS are in low Earth orbit, flying 550 and 400 km above the ground, respectively. We choose $D = 550$ km in Eq. (31). Note that, after the dark photon decays, the resulting charged particles are bent in the Earth's magnetic field by an angle

$$\theta = 0.5° \, \frac{\mathrm{TeV}}{p} \, \frac{L}{550 \text{ km}} \, \frac{B}{0.5 \text{ G}} \; , \tag{33}$$

where p is the particle's momentum, L is the distance it travels, and we have normalized the Earth's magnetic field B to an average value at the surface of the Earth. For $m_X \gtrsim$ TeV, this deflection is less than the dispersion from the dark matter's spatial distribution at the center of the Earth given in Eq. (28), but for $m_X \sim 100$ GeV, this deflection may be significant, and the signal may arrive at an angle as large as $5°$ relative to straight down.

The resulting event rates for such space-based detectors are given in Fig. 7 for a live

16

time of 10 years. For $m_X \lesssim 100$ GeV, the parameter space that can be probed largely overlaps with that already probed by direct detection, but Fermi and AMS may set bounds complementary to the existing direct detection experiments. For higher masses one may probe unexplored regions in the dark photon parameter space reaching $m_{A'} \sim \mathcal{O}(1)$ GeV between $\varepsilon \sim 10^{-8}$ and 10^{-7}. As a benchmark, consider the parameters $m_X = 1$ TeV, $m_{A'} = 830$ MeV, and $\varepsilon = 3 \times 10^{-8}$, for which one expects $N_{\mathrm{sig}} = 10$ signal events in 10 live years. The velocity difference and opening angle distributions are shown in the center panels of Figs. 5 and 6. For a primary propagation distance of ~ 300 km, this yields timing separations of up to tens of nanoseconds and separations of up to a kilometer. We therefore do not expect to see both primary particles from dark photon decay in Fermi or AMS. Of course, this is still possible: the A' may decay near Fermi or AMS; secondary photons from hadronic final states my happen to have little transverse momentum; or the A' may decay far from the detectors to two charged particles, which are both bent by the magnetic field into the detectors. Although possible, all of these are highly improbable, and two-particle events are a small fraction of the total number of single-particle signal events. An alternative possibility is when there is a small splitting between $m_{A'}$ and $2m_f$. In this case the decay products have small transverse momentum by Eq. (29), at the cost of a reduced branching ratio.

Last, the number of signal events N_{sig} does not take into account experimental efficiencies associated with each apparatus. For example, we have assumed that the volume of the International Space Station between the Earth and AMS does not affect the dark photon primaries, and, further, that the hadronic products of the dark photons are detectable. A more complete analysis of the Fermi/AMS reach will require more realistic modeling and different triggers.

V. CONCLUSIONS

We have presented a novel method to discover dark matter that interacts with the known particles through dark photons that kinetically mix with the SM photon. The dark matter is captured by the Earth and thermalized in the Earth's center, and then annihilates to dark photons. The dark photons then travel to near the surface of the Earth and decay. We have determined the signal rates without simplifying assumptions concerning the dark matter and dark photon masses. In viable regions of the model parameter space, thousands of such dark photon decays are possible in IceCube, and smaller, but still detectable, signals in space-based detectors such as Fermi and AMS are also possible.

As with traditional indirect detection signals that rely on annihilation to neutrinos, the dark photon signal points back to the center of the Earth, differentiating it from astrophysical backgrounds. In contrast to the neutrino signal, however, the dark photon decays to two visible particles. The dark photon signal is therefore even more striking, as it is monoenergetic if fully contained. In addition, in principle both particles could be detected simultaneously yielding, for example, parallel muon tracks in IceCube with separations of $\sim \mathcal{O}(10 \text{ m})$. We have shown distributions of these separations for representative points in model parameter space.

As discussed in Sec. III A, the leading uncertainty in the signal rate predictions is from the capture rate analysis. The escape velocity of the Earth is not large, and so this capture rate is subject to detailed modeling, including the effects of the Earth, Sun, Jupiter, and Venus. In addition, a cold "dark disk" population of dark matter may significantly enhance the

capture rates. The implications of these effects for WIMP dark matter have been considered in Refs. [20–24, 56]; it would be interesting to determine their effects on dark matter with dark photon-mediated interactions.

In this study, we have assumed the dark matter X is a Dirac fermion and the mediator is a dark photon that mixes only with the SM photon, and so couples only to charged particles. It would be interesting to consider cases where X is a pseudo-Dirac fermion or a scalar, and cases where the dark photon mixes with the Z (and so couples to neutrinos, for example), or is replaced by a scalar (for which the dark matter may also be Majorana). Dark matter that collects and annihilates at the center of the Sun is also a promising source of decaying dark photons and will probe different regions of parameter space [88].

Finally, the experiments have been modeled very roughly here; detailed analyses, preferably by the experimental collaborations themselves, are required to evaluate the accuracy of the signal rate estimates. However, our conclusion that there are viable regions of parameter space that predict thousands of signal events indicates that there are certainly regions of parameter space where the indirect detection signals discussed here are the most sensitive probes, surpassing direct detection detectors, beam dump experiments, and cosmological probes. The possibility of discovering signals of dark matter that, unlike so many other indirect detection signals, are essentially free of difficult-to-quantify astrophysical backgrounds, provides a strong motivation for these searches.

VI.   ACKNOWLEDGMENTS

Appendix: Decay Product Distributions

We summarize analytic results for the kinematic distributions of the dark photon decay products, presenting the forward velocity difference between the two final states and the lab frame opening angle, which may be used to determine the time delay and track separation between these objects in a detector. For simplicity, we assume the dark photon decays isotropically in its rest frame. Angular correlations will modify our distributions, but will not change the ranges of time delay and track separation, which are our primary interest. With this approximation, in the center-of-mass frame, the dark photon decay products are evenly distributed in $\cos\theta_{\text{CM}}$, where θ_{CM} is the angle between the dark photon boost direction and one of the decay products. The value of a kinematic quantity k for fixed model

18
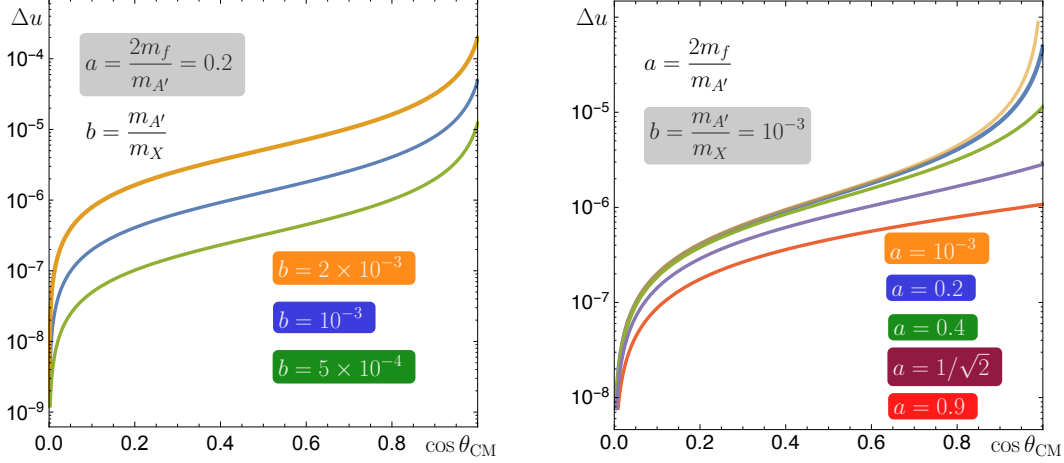
FIG. 8: Velocity difference, Δu, of the two particles produced in A' decay as a function of the center-of-mass frame angle $\cos\theta_{\mathrm{CM}}$ for representative values of a and b.

parameters is a function κ of $\cos\theta_{\mathrm{CM}}$. The distribution of these values f is

$$f(k) = \sum_{\cos\theta_{\mathrm{CM}}^i}^{\kappa(\cos\theta_{\mathrm{CM}}^i)=k} \frac{1}{|\kappa'(\cos\theta_{\mathrm{CM}}^i)|} \; . \tag{A.1}$$

Throughout this appendix we consider two-body decays $A' \to f\bar{f}$ and define

$$a = \frac{2m_f}{m_{A'}} \qquad\qquad b = \frac{m_{A'}}{m_X} \; . \tag{A.2}$$

1. Velocity Distribution and Time Delay

In the Earth's rest frame, the forward velocities of the particles produced in A' decay are

$$u_{\pm} = \frac{\sqrt{1-b^2} \pm \sqrt{1-a^2}\cos\theta_{\mathrm{CM}}}{1 \pm \sqrt{1-b^2}\sqrt{1-a^2}\cos\theta_{\mathrm{CM}}} \; , \tag{A.3}$$

where we use natural units $c = 1$. The difference of these velocities is

$$\Delta u \equiv u_+ - u_- = \frac{2b^2\sqrt{1-a^2}\cos\theta_{\mathrm{CM}}}{1-(1-b^2)(1-a^2)\cos^2\theta_{\mathrm{CM}}} \approx \frac{2b^2\sqrt{1-a^2}\cos\theta_{\mathrm{CM}}}{1-(1-a^2)\cos^2\theta_{\mathrm{CM}}} \; , \tag{A.4}$$

where the last expression is valid for $b \ll 1$, the values we are most interested in. We plot $\Delta u(\cos\theta_{\mathrm{CM}})$ in Fig. 8. Observe that Δu scales like b^2 for small b; this is also seen in Fig. 5, where the $m_X = 1$ TeV and $m_X = 10$ TeV plots are related by a simple rescaling. Further, the distribution is fairly insensitive to $a = 2m_\ell/m_{A'}$ for $m_{A'} \sim$ GeV and for $\ell = e, \mu$.

For a given Δu, the (dimensionful) time delay between the two decay products for a decay that occurs a distance L from the detection point is

$$\Delta t = \frac{L}{cu_-} - \frac{L}{cu_+} = \frac{L\Delta u}{cu_- u_+} \approx \frac{L}{c}\Delta u \; , \tag{A.5}$$

where we've taken the limit of large boost so that $u_{\pm} \to 1$.

19
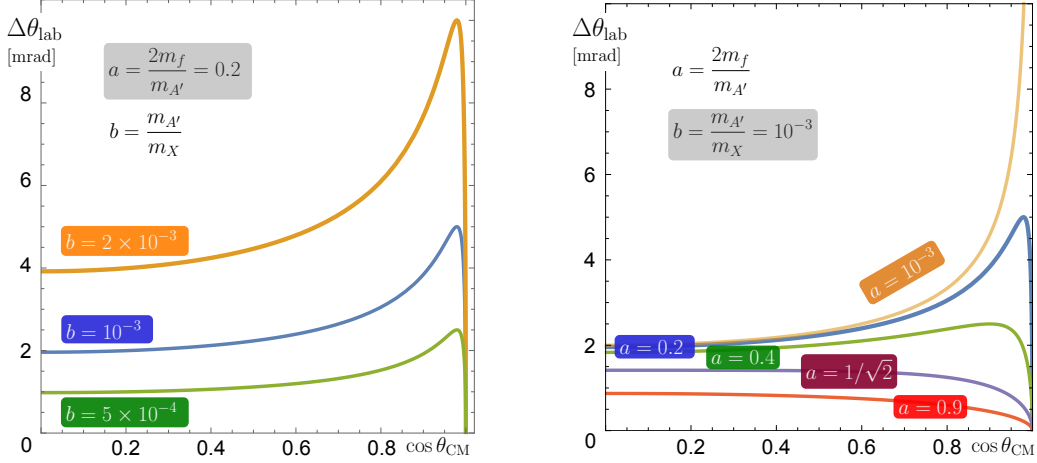
FIG. 9: Earth-frame opening angle between the two particles produced in A' decay as a function of the center-of-mass frame angle $\cos\theta_{\mathrm{CM}}$ for representative values of a and b.

2. Opening Angle and Track Separation

In the Earth's rest frame, the angles $\theta_\pm$ of the decay products relative to the A' decay direction are

$$\tan\theta_\pm = \frac{\pm b\sqrt{1-a^2}\sin\theta_{\mathrm{CM}}}{\sqrt{1-b^2}\pm\sqrt{1-a^2}\cos\theta_{\mathrm{CM}}} . \tag{A.6}$$

The opening angle between the two decay products is therefore

$$\Delta\theta_{\mathrm{lab}} \equiv \tan^{-1}\theta_+ - \tan^{-1}\theta_- \approx \frac{2b\sqrt{1-a^2}\sin\theta_{\mathrm{CM}}}{1-(1-a^2)\cos^2\theta_{\mathrm{CM}}} , \tag{A.7}$$

where the last expression is valid for $b \ll 1$. The scaling $\Delta\theta_{\mathrm{lab}} \propto b$ can be seen in the center and right plots in Fig. 6. The maximal opening angle is

$$\Delta\theta_{\mathrm{lab}}^{\mathrm{max}} = \begin{cases} 2b\sqrt{1-a^2} & \text{at } \cos\theta_{\mathrm{CM}} = 0 , \quad a \geq \dfrac{1}{\sqrt{2}} \\[2ex] \dfrac{b}{a} & \text{at } \cos\theta_{\mathrm{CM}} = \sqrt{\dfrac{1-2a^2}{1-a^2}} , \quad a < \dfrac{1}{\sqrt{2}} \end{cases} . \tag{A.8}$$

We plot $\Delta\theta_{\mathrm{lab}}(\cos\theta_{\mathrm{CM}})$ in Fig. 9. For large a, the opening angle is maximized at $\cos\theta_{\mathrm{CM}} = 0$, consistent with the intuition that the largest opening angle should correspond to fully transverse decays in the center-of-mass frame. But for small a, this intuition does not hold: the maximal opening angle occurs for $\cos\theta_{\mathrm{CM}} \approx 1$, where one particle is emitted "backwards" in the A' center-of-mass frame so that its forward velocity is significantly reduced, enlarging the opening angle. In most of the range of $\cos\theta_{\mathrm{CM}}$, $\Delta\theta_{\mathrm{lab}} \approx 2b$, but the maximal opening angle $\Delta\theta_{\mathrm{lab}}^{\mathrm{max}} \approx b/a$ occurs for large $\cos\theta_{\mathrm{CM}} \approx 1 - \frac{1}{2}a^2$.

Finally we show the correlation between $\Delta\theta_{\mathrm{lab}}$ and Δu in Fig. 10. These plots identify where one may use the combination of the opening angle and time delay to discriminate the two final state particles.

20
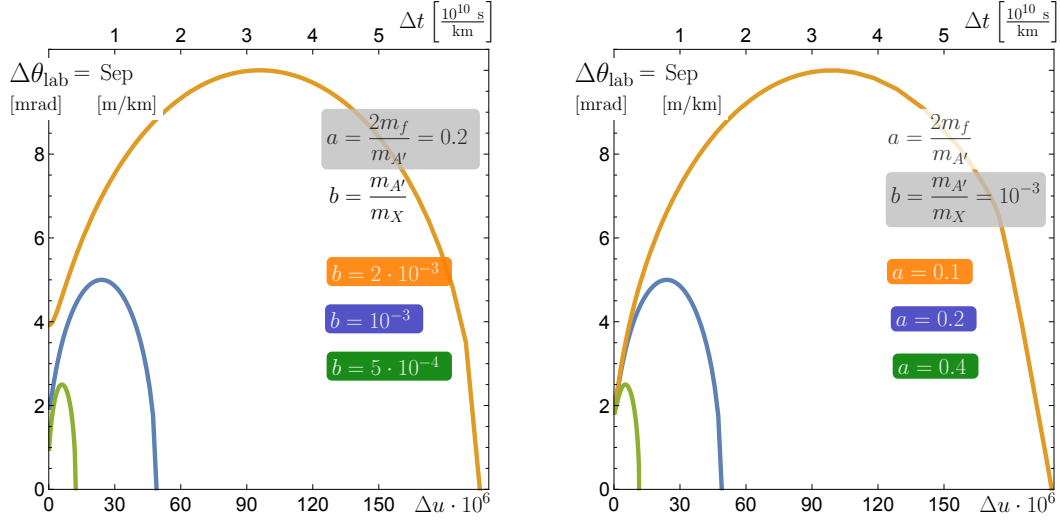
FIG. 10: The correlation between the velocity difference and the lab-frame opening angle of the two particles produced in A' decay for representative values of a and b.

[1] I. Y. Kobzarev, L. Okun, and I. Y. Pomeranchuk, "On the possibility of experimental observation of mirror particles," *Sov.J.Nucl.Phys.* **3** (1966) 837–841.

[2] L. B. Okun, "Limits of Electrodynamics: Paraphotons?," *Sov. Phys. JETP* **56** (1982) 502. [Zh. Eksp. Teor. Fiz.83,892(1982)].

[3] B. Holdom, "Two U(1)'s and Epsilon Charge Shifts," *Phys.Lett.* **B166** (1986) 196.

[4] B. Holdom, "Searching for ϵ Charges and a New U(1)," *Phys. Lett.* **B178** (1986) 65.

[5] R. Essig *et al.*, "Working Group Report: New Light Weakly Coupled Particles," in *Community Summer Study 2013: Snowmass on the Mississippi (CSS2013) Minneapolis, MN, USA, July 29-August 6, 2013*. 2013. `arXiv:1311.0029 [hep-ph]`.

[6] R. Foot, "Mirror dark matter: Cosmology, galaxy structure and direct detection," *Int.J.Mod.Phys.* **A29** (2014) 1430013, `arXiv:1401.3965 [astro-ph.CO]`.

[7] K. Freese, "Can Scalar Neutrinos Or Massive Dirac Neutrinos Be the Missing Mass?," *Phys. Lett.* **B167** (1986) 295.

[8] W. H. Press and D. N. Spergel, "Capture by the Sun of a Galactic Population of Weakly Interacting Massive Particles," *Astrophys.J.* **296** (1985) 679–684.

[9] J. Silk, K. A. Olive, and M. Srednicki, "The Photino, the Sun and High-Energy Neutrinos," *Phys. Rev. Lett.* **55** (1985) 257–259.

[10] L. M. Krauss, M. Srednicki, and F. Wilczek, "Solar System Constraints and Signatures for Dark Matter Candidates," *Phys. Rev.* **D33** (1986) 2079–2083.

[11] K. Griest and D. Seckel, "Cosmic Asymmetry, Neutrinos and the Sun," *Nucl.Phys.* **B283** (1987) 681.

[12] T. K. Gaisser, G. Steigman, and S. Tilav, "Limits on Cold Dark Matter Candidates from Deep Underground Detectors," *Phys. Rev.* **D34** (1986) 2206.

[13] A. Gould, "WIMP Distribution in and Evaporation From the Sun," *Astrophys.J.* **321** (1987) 560.

[14] A. Gould, "Resonant Enhancements in WIMP Capture by the Earth," *Astrophys.J.* **321**

(1987) 571.

[15] A. Gould, "Direct and indirect capture of weakly interacting massive particles by the earth," *Astrophys. J.* **328** (May, 1988) 919–939.

[16] A. Gould, "Cosmological density of WIMPs from solar and terrestrial annihilations," *Astrophys.J.* **388** (1992) 338–344.

[17] T. Damour and L. M. Krauss, "A New solar system population of WIMP dark matter," *Phys. Rev. Lett.* **81** (1998) 5726–5729, `arXiv:astro-ph/9806165 [astro-ph]`.

[18] T. Damour and L. M. Krauss, "A New WIMP population in the solar system and new signals for dark matter detectors," *Phys. Rev.* **D59** (1999) 063509, `arXiv:astro-ph/9807099 [astro-ph]`.

[19] A. Gould and S. M. Khairul Alam, "Can heavy WIMPs be captured by the earth?," *Astrophys. J.* **549** (2001) 72–75, `arXiv:astro-ph/9911288 [astro-ph]`.

[20] J. Lundberg and J. Edsjo, "WIMP diffusion in the solar system including solar depletion and its effect on earth capture rates," *Phys. Rev.* **D69** (2004) 123505, `arXiv:astro-ph/0401113 [astro-ph]`.

[21] A. H. G. Peter, "Dark matter in the solar system I: The distribution function of WIMPs at the Earth from solar capture," *Phys. Rev.* **D79** (2009) 103531, `arXiv:0902.1344 [astro-ph.HE]`.

[22] A. H. G. Peter, "Dark matter in the solar system II: WIMP annihilation rates in the Sun," *Phys. Rev.* **D79** (2009) 103532, `arXiv:0902.1347 [astro-ph.HE]`.

[23] A. H. G. Peter, "Dark matter in the solar system III: The distribution function of WIMPs at the Earth from gravitational capture," *Phys. Rev.* **D79** (2009) 103533, `arXiv:0902.1348 [astro-ph.HE]`.

[24] T. Bruch, A. H. G. Peter, J. Read, L. Baudis, and G. Lake, "Dark Matter Disc Enhanced Neutrino Fluxes from the Sun and Earth," *Phys. Lett.* **B674** (2009) 250–256, `arXiv:0902.4001 [astro-ph.HE]`.

[25] S. M. Koushiappas and M. Kamionkowski, "Galactic Substructure and Energetic Neutrinos from the Sun and the Earth," *Phys. Rev. Lett.* **103** (2009) 121301, `arXiv:0907.4778 [astro-ph.CO]`.

[26] C. Delaunay, P. J. Fox, and G. Perez, "Probing Dark Matter Dynamics via Earthborn Neutrinos at IceCube," *JHEP* **05** (2009) 099, `arXiv:0812.3331 [hep-ph]`.

[27] P. Schuster, N. Toro, and I. Yavin, "Terrestrial and Solar Limits on Long-Lived Particles in a Dark Sector," *Phys. Rev.* **D81** (2010) 016002, `arXiv:0910.1602 [hep-ph]`.

[28] P. Schuster, N. Toro, N. Weiner, and I. Yavin, "High Energy Electron Signals from Dark Matter Annihilation in the Sun," *Phys. Rev.* **D82** (2010) 115012, `arXiv:0910.1839 [hep-ph]`.

[29] P. Meade, S. Nussinov, M. Papucci, and T. Volansky, "Searches for Long Lived Neutral Particles," *JHEP* **06** (2010) 029, `arXiv:0910.4160 [hep-ph]`.

[30] B. Batell, M. Pospelov, A. Ritz, and Y. Shang, "Solar Gamma Rays Powered by Secluded Dark Matter," *Phys. Rev.* **D81** (2010) 075004, `arXiv:0910.1567 [hep-ph]`.

[31] **The Fermi LAT** Collaboration, M. Ajello *et al.*, "Constraints on Dark Matter Models from a Fermi Lat Search for High-Energy Cosmic-Ray Electrons from the Sun," *Phys. Rev.* **D84** (2011) 032007, `arXiv:1107.4272 [astro-ph.HE]`.

[32] I. F. M. Albuquerque, C. Perez de Los Heros, and D. S. Robertson, "Constraints on self interacting dark matter from IceCube results," *JCAP* **1402** (2014) 047, `arXiv:1312.0797 [astro-ph.CO]`.

[33] J. Chen, Z.-L. Liang, Y.-L. Wu, and Y.-F. Zhou, "Long-Range Self-Interacting Dark Matter in the Sun," `arXiv:1505.04031 [hep-ph]`.

[34] J. Berger, Y. Cui, and Y. Zhao, "Detecting Boosted Dark Matter from the Sun with Large Volume Neutrino Detectors," *JCAP* **1502** (2015) 005, `arXiv:1410.2246 [hep-ph]`.

[35] M. Vogelsberger, J. Zavala, and A. Loeb, "Subhaloes in Self-Interacting Galactic Dark Matter Haloes," *Mon. Not. R. Astron. Soc.* **423** (2012) 3740, `arXiv:1201.5892 [astro-ph.CO]`.

[36] M. Rocha, A. H. G. Peter, J. S. Bullock, M. Kaplinghat, S. Garrison-Kimmel, J. Onorbe, and L. A. Moustakas, "Cosmological Simulations with Self-Interacting Dark Matter I: Constant Density Cores and Substructure," *Mon. Not. R. Astron. Soc.* **430** (2013) 81–104, `arXiv:1208.3025 [astro-ph.CO]`.

[37] A. H. G. Peter, M. Rocha, J. S. Bullock, and M. Kaplinghat, "Cosmological Simulations with Self-Interacting Dark Matter Ii: Halo Shapes Vs. Observations," *Mon. Not. R. Astron. Soc.* **430** (2013) 105, `arXiv:1208.3026 [astro-ph.CO]`.

[38] J. Zavala, M. Vogelsberger, and M. G. Walker, "Constraining Self-Interacting Dark Matter with the Milky Way's Dwarf Spheroidals," *Mon. Not. R. Astro. Soc.* **431** (2013) L20–L24, `arXiv:1211.6426 [astro-ph.CO]`.

[39] S. Tulin, H.-B. Yu, and K. M. Zurek, "Beyond Collisionless Dark Matter: Particle Physics Dynamics for Dark Matter Halo Structure," *Phys. Rev.* **D87** (2013) 115007, `arXiv:1302.3898 [hep-ph]`.

[40] M. Collie and R. Foot, "Neutrino masses in the SU(5) x SU(5)-prime mirror symmetric model," *Phys.Lett.* **B432** (1998) 134–138, `arXiv:hep-ph/9803261 [hep-ph]`.

[41] M. Kaplinghat, T. Linden, and H.-B. Yu, "Galactic Center Excess in γ Rays from Annihilation of Self-Interacting Dark Matter," *Phys. Rev. Lett.* **114** (2015) 211303, `arXiv:1501.03507 [hep-ph]`.

[42] J. A. Adams, S. Sarkar, and D. W. Sciama, "CMB anisotropy in the decaying neutrino cosmology," *Mon. Not. Roy. Astron. Soc.* **301** (1998) 210–214, `arXiv:astro-ph/9805108 [astro-ph]`.

[43] X.-L. Chen and M. Kamionkowski, "Particle decays during the cosmic dark ages," *Phys. Rev.* **D70** (2004) 043502, `arXiv:astro-ph/0310473 [astro-ph]`.

[44] N. Padmanabhan and D. P. Finkbeiner, "Detecting dark matter annihilation with CMB polarization: Signatures and experimental prospects," *Phys. Rev.* **D72** (2005) 023508, `arXiv:astro-ph/0503486 [astro-ph]`.

[45] T. R. Slatyer, "Indirect Dark Matter Signatures in the Cosmic Dark Ages I. Generalizing the Bound on s-wave Dark Matter Annihilation from Planck," `arXiv:1506.03811 [hep-ph]`.

[46] M. Buschmann, J. Kopp, J. Liu, and P. A. N. Machado, "Lepton Jets from Radiating Dark Matter," *JHEP* **07** (2015) 045, `arXiv:1505.07459 [hep-ph]`.

[47] A. R. Zentner, "High-Energy Neutrinos From Dark Matter Particle Self-Capture Within the Sun," *Phys. Rev.* **D80** (2009) 063501, `arXiv:0907.3448 [astro-ph.HE]`.

[48] P. Baratella, M. Cirelli, A. Hektor, J. Pata, M. Piibeleht, *et al.*, "PPPC 4 DM ν: a Poor Particle Physicist Cookbook for Neutrinos from Dark Matter Annihilations in the Sun," *JCAP* **1403** (2014) 053, `arXiv:1312.6408 [hep-ph]`.

[49] N. Fornengo, P. Panci, and M. Regis, "Long-Range Forces in Direct Dark Matter Searches," *Phys. Rev.* **D84** (2011) 115002, `arXiv:1108.4661 [hep-ph]`.

[50] J. Lewin and P. Smith, "Review of Mathematics, Numerical Factors, and Corrections for Dark Matter Experiments Based on Elastic Nuclear Recoil," *Astropart.Phys.* **6** (1996)

87–112.

[51] A. M. Dziewonski and D. L. Anderson, "Preliminary reference Earth model," *Physics of The Earth and Planetary Interiors* **25** (1981) 297–356.

[52] H. D. Holland and K. K. Turekian, *Treatise on Geochemistry.* Pergamon [Imprint], 2003.

[53] A. Gould, "Gravitational diffusion of solar system WIMPs," *ApJ* **368** (1991) 610–615.

[54] J. I. Read, L. Mayer, A. M. Brooks, F. Governato, and G. Lake, "A dark matter disc in three cosmological simulations of Milky Way mass galaxies," *Mon. Not. R. Astro. Soc.* **397** (2009) 44–51, `arXiv:0902.0009`.

[55] J. I. Read, G. Lake, O. Agertz, and V. P. Debattista, "Thin, thick and dark discs in ΛCDM," *Mon. Not. R. Astro. Soc.* **389** (2008) 1041–1057, `arXiv:0803.2714`.

[56] C. W. Purcell, J. S. Bullock, and M. Kaplinghat, "The Dark Disk of the Milky Way," *Astrophys. J.* **703** (2009) 2275–2284, `arXiv:0906.5348 [astro-ph.GA]`.

[57] A. Peter, "Dark Matter Bound to the Solar System: Consequences for Annihilation Searches," in *Proceedings, 44Th Rencontres De Moriond on Electroweak Interactions and Unified Theories*, pp. 359–366. 2009. `arXiv:0905.2456 [astro-ph.HE]`.

[58] J. D. Vergados, "Modulation effect in the differential rate for supersymmetric dark matter detection," *Phys. Rev.* **D58** (1998) 103001, `arXiv:hep-ph/9802253 [hep-ph]`.

[59] M. Vogelsberger, A. Helmi, V. Springel, S. D. White, J. Wang, *et al.*, "Phase-Space Structure in the Local Dark Matter Distribution and Its Signature in Direct Detection Experiments," *Mon. Not. R. Astron. Soc.* **395** (2009) 797–811, `arXiv:0812.0362 [astro-ph]`.

[60] M. Fairbairn and T. Schwetz, "Spin-Independent Elastic WIMP Scattering and the Dama Annual Modulation Signal," *JCAP* **0901** (2009) 037, `arXiv:0808.0704 [hep-ph]`.

[61] M. Kuhlen, N. Weiner, J. Diemand, P. Madau, B. Moore, *et al.*, "Dark Matter Direct Detection with Non-Maxwellian Velocity Structure," *JCAP* **1002** (2010) 030, `arXiv:0912.2358 [astro-ph.GA]`.

[62] F. Ling, E. Nezri, E. Athanassoula, and R. Teyssier, "Dark Matter Direct Detection Signals Inferred from a Cosmological N-Body Simulation with Baryons," *JCAP* **1002** (2010) 012, `arXiv:0909.2028 [astro-ph.GA]`.

[63] M. Lisanti, L. E. Strigari, J. G. Wacker, and R. H. Wechsler, "The Dark Matter at the End of the Galaxy," *Phys. Rev.* **D83** (2011) 023519, `arXiv:1010.4300 [astro-ph.CO]`.

[64] Y.-Y. Mao, L. E. Strigari, R. H. Wechsler, H.-Y. Wu, and O. Hahn, "Halo-To-Halo Similarity and Scatter in the Velocity Distribution of Dark Matter," *Astrophys.J.* **764** (2013) 35, `arXiv:1210.2721 [astro-ph.CO]`.

[65] K. Choi, C. Rott, and Y. Itow, "Impact of the Dark Matter Velocity Distribution on Capture Rates in the Sun," *JCAP* **1405** (2014) 049, `arXiv:1312.0273 [astro-ph.HE]`.

[66] M. Abramowitz and I. Stegun, *Handbook of Mathematical Functions: With Formulas, Graphs, and Mathematical Tables.* Applied mathematics series. Dover Publications, 1964.

[67] J. Liu, N. Weiner, and W. Xue, "Signals of a Light Dark Force in the Galactic Center," *JHEP* **08** (2015) 050, `arXiv:1412.1485 [hep-ph]`.

[68] A. Sommerfeld, "Über die Beugung und Bremsung der Elektronen," *Ann. der Physik* **403** (1931) 257.

[69] S. Cassel, "Sommerfeld factor for arbitrary partial wave processes," *J.Phys.* **G37** (2010) 105009, `arXiv:0903.5307 [hep-ph]`.

[70] T. R. Slatyer, "The Sommerfeld enhancement for dark matter with an excited state," *JCAP* **1002** (2010) 028, `arXiv:0910.5713 [hep-ph]`.

[71] J. L. Feng, M. Kaplinghat, and H.-B. Yu, "Sommerfeld Enhancements for Thermal Relic

Dark Matter," *Phys. Rev.* **D82** (2010) 083525, `arXiv:1005.4678 [hep-ph]`.

[72] **IceCube** Collaboration, R. Abbasi *et al.*, "The Design and Performance of IceCube DeepCore," *Astropart. Phys.* **35** (2012) 615–624, `arXiv:1109.6096 [astro-ph.IM]`.

[73] E. Del Nobile, M. Kaplinghat, and H.-B. Yu, "Direct Detection Signatures of Self-Interacting Dark Matter with a Light Mediator," `arXiv:1507.04007 [hep-ph]`.

[74] J. B. Dent, F. Ferrer, and L. M. Krauss, "Constraints on Light Hidden Sector Gauge Bosons from Supernova Cooling," `arXiv:1201.2683 [astro-ph.CO]`.

[75] H. K. Dreiner, J.-F. Fortin, C. Hanhart, and L. Ubaldi, "Supernova constraints on MeV dark sectors from e^+e^- annihilations," *Phys. Rev.* **D89** (2014) 105015, `arXiv:1310.3826 [hep-ph]`.

[76] D. Kazanas, R. N. Mohapatra, S. Nussinov, V. L. Teplitz, and Y. Zhang, "Supernova Bounds on the Dark Photon Using its Electromagnetic Decay," *Nucl.Phys.* **B890** (2014) 17–29, `arXiv:1410.0221 [hep-ph]`.

[77] E. Rrapaj and S. Reddy, "Nucleon-nucleon bremsstrahlung of dark gauge bosons and revised supernova constraints," `arXiv:1511.09136 [nucl-th]`.

[78] **LUX** Collaboration, D. S. Akerib *et al.*, "First Results from the Lux Dark Matter Experiment at the Sanford Underground Research Facility," *Phys. Rev. Lett.* **112** (2014) 091303, `arXiv:1310.8214 [astro-ph.CO]`.

[79] M. Kaplinghat, S. Tulin, and H.-B. Yu, "Direct Detection Portals for Self-interacting Dark Matter," *Phys. Rev.* **D89** (2014) 035009, `arXiv:1310.7945 [hep-ph]`.

[80] H. An, M. Pospelov, J. Pradler, and A. Ritz, "Direct Detection Constraints on Dark Photon Dark Matter," *Phys. Lett.* **B747** (2015) 331–338, `arXiv:1412.8378 [hep-ph]`.

[81] J. Billard, L. Strigari, and E. Figueroa-Feliciano, "Implication of Neutrino Backgrounds on the Reach of Next Generation Dark Matter Direct Detection Experiments," *Phys. Rev.* **D89** (2014) no. 2, 023524, `arXiv:1307.5458 [hep-ph]`.

[82] **Particle Data Group** Collaboration, K. A. Olive *et al.*, "Review of Particle Physics," *Chin. Phys.* **C38** (2014) 090001.

[83] I. Albuquerque, G. Burdman, and Z. Chacko, "Neutrino telescopes as a direct probe of supersymmetry breaking," *Phys. Rev. Lett.* **92** (2004) 221802, `arXiv:hep-ph/0312197 [hep-ph]`.

[84] I. F. M. Albuquerque, G. Burdman, and Z. Chacko, "Direct detection of supersymmetric particles in neutrino telescopes," *Phys. Rev.* **D75** (2007) 035006, `arXiv:hep-ph/0605120 [hep-ph]`.

[85] S. Kopper, "Search for Neutrino-Induced Double Tracks as an Exotic Physics Signature in IceCube," *Proceedings of 'The 34th International Cosmic Ray Conference'* (2015) . PoS (ICRC2015) 1104.

[86] F. Halzen and S. R. Klein, "Icecube: an Instrument for Neutrino Astronomy," *Rev.Sci.Instrum.* **81** (2010) 081101, `arXiv:1007.1247 [astro-ph.HE]`.

[87] **IceCube PINGU** Collaboration, M. G. Aartsen *et al.*, "Letter of Intent: The Precision IceCube Next Generation Upgrade (PINGU)," `arXiv:1401.2046 [physics.ins-det]`.

[88] J. L. Feng, J. Smolinsky, and P. Tanedo. work in progress.

[89] Wolfram Research, Inc., *Mathematica, Version 10.2.* Champaign, Illinois, 2015.